https://doi.org/10.5194/mr-2026-7
Preprint. Discussion started: 2 April 2026

Open Access MAGNETIC RESONANCE Discussions

Optimally controlled NMR in electrochemistry: Larmor and nutation frequency selective spin excitation for locally selective NMR experiments

Johannes F. Kochs[1,2,*], Armin J. Römer[1,2,*], Michael Schatz[1], Matthias Streun[3], Sven Jovanovic[1], Rüdiger-A. Eichel[1,4,5], Simone S. Köcher[1,6], and Josef Granwehr[1,2]

[1]Forschungszentrum Jülich GmbH, Institute of Energy Technologies, Fundamental Electrochemistry (IET-1), Jülich, Germany
[2]Institute of Technical and Macromolecular Chemistry, RWTH Aachen University, Aachen, Germany
[3]Forschungszentrum Jülich GmbH, Institute of Technology and Engineering (ITE), Jülich, Germany
[4]Institute of Physical Chemistry, RWTH Aachen University, Aachen, Germany
[5]Faculty of Mechanical Engineering, RWTH Aachen University, Aachen, Germany
[6]Fritz Haber Institute of the Max Planck Society, Berlin, Germany

Correspondence: Simone S. Köcher (s.koecher@fz-juelich.de)

Abstract. Spectroelectrochemical nuclear magnetic resonance (NMR) experiments are faced with numerous challenges originating from shielding effects and susceptibility gradients in samples, leading to inhomogeneous static magnetic fields B_0 and radio frequency (rf) fields B_1. Moreover, magnetic feedback caused by eddy currents in conductors can obstruct precise measurements. Previous works have shown that these eddy current induced magnetic field distortions can be accurately predicted by finite element method (FEM) simulations. In this work, we present a workflow combining FEM predictions with quantum optimal control (QOC) to tailor custom NMR pulses that exploit specific magnetic field distortions for selective excitation of affected sample regions. The desired selectivity was achieved using pattern pulses optimized for a particular B_1 or Larmor frequency ν_0. Experimental validation was performed on a heterogeneous phantom consisting of two cavities filled with two spectroscopically distinguishable liquids, one between copper disks to mimic an electrochemical cell, and one between polymer disks as reference. An over 30-fold suppression of the reference resonance in between polymer compared to the resonance in between copper disks was achieved, demonstrating how QOC-tailored pulses can selectively address FEM-predicted B_1 distortions to achieve spatial selectivity. It was also demonstrated how QOC-tailored pulses can selectively excite specific ν_0 despite of B_0 distortions, which implies that difficulties with conventional solvent suppression techniques in electrochemical setups can be mitigated using the adjustable robustness of QOC-tailored pulses. The presented approach sets the stage for gradient-free, localized in operando NMR in electrochemistry and material sciences, with the prospect of surface selectivity down to the detection limit of the setup.

1 Introduction

Spectroelectrochemical methods offer valuable, non-invasive in situ and in operando insights into electrochemical transformation processes, such as electrolysis and electrocatalysis. More advanced techniques pave the way to study crystallographic

https://doi.org/10.5194/mr-2026-7
Preprint. Discussion started: 2 April 2026

Open Access MAGNETIC RESONANCE Discussions

(Bommarito et al., 1992; Huang et al., 2018) and optical (Williamson et al., 2003; Holtz et al., 2014) properties, concentrations (Corson et al., 2020; Jovanovic et al., 2021), chemical environment (Corson et al., 2020; Faid et al., 2020), and metal coordination (Lee et al., 2022) within operating electrochemical cells. A fitting cell design depending on the applied technique is important to optimize accessibility for spectroscopic investigations, i.e. thin layer cells to minimize solvent and background signal (Zoski, 2007). Spectroelectrochemical nuclear magnetic resonance (NMR) investigations offer additional flexibility through customizing the employed pulse sequences for a given experiment. However, conducting reliable NMR experiments on entire electrochemical cell setups, yielding credible, informative results about electrochemical transformation processes, raises several challenges.

Firstly, incorporating an entire electrochemical setup in an NMR tube including several electrodes (working, counter, reference), liquid electrolyte, and current collectors, while maintaining electric contact for applying a potential, requires custom-designed setups. A large variety of cell setups have been designed for electrochemical applications, ranging from flow mode and batch mode cells in 5 mm NMR tubes (Richards and Evans, 1975; Jovanovic et al., 2021) to custom battery housings (Pecher et al., 2017; Wolff et al., 2025) and commercial coin cell NMR setups (Walder et al., 2021). Schatz et al. (2022) followed a compromise approach by assembling a flexible NMR setup that yielded reproducible results while simultaneously being easily replicable without demanding special equipment.

Secondly, electrochemical transformation processes are predominantly located at interfaces and their effectiveness is defined by electrochemical reaction rates, reaction mechanisms as well as adsorption processes (Hamann and Vielstich, 2005). Standard NMR lacks selectivity and its sensitivity is strained to detect surface species, compounded further by a signal that is mostly dominated by solvent and bulk species. While using conventional solvent suppression sequences to minimize solvent signals (McKay, 2009) is challenging in the presence of electrically conductive electrode components, reasonable spacial selectivity was achieved by magnetic resonance imaging (MRI) pulse sequences based on magnetic field gradients for spatial encoding via frequency or phase (Schatz et al., 2023). However, MRI experiments are limited by a compromise between spatial, spectral, and temporal resolution.

Finally, electrochemical cells contain several metallic elements. Electrical conductors distort both the static B_0 and oscillating B_1 field that NMR relies on, which results in reduced resolution, non-quantitative results, and potential artifacts. However, the local field distortions can be assessed qualitatively and quantitatively by numerical finite-element-method (FEM) simulations, which are crucial for successful, robust in operando NMR cell development. FEM-based investigations of B_0 and B_1 fields around electric conductors have correctly reproduced experimental findings of B_1 field distortions due to the metallic skin effect (Ilott and Jerschow, 2017; Mohammadi and Jerschow, 2019), as well as the dependence of B_1 distortions on the orientation of the conductor (Ilott et al., 2014; Vashaee et al., 2015; Jovanovic et al., 2021).

FEM simulations have also been utilized to validate and optimize uniform B_1 distribution within in operando cell setups to study PEM fuel cells (Zhang et al., 2011), as well as battery applications, (Aguilera et al., 2021; Sanders et al., 2022) up to commercial coin cell scales (Walder et al., 2021). Most recently, Schatz et al. (2024) presented a workflow to integrate FEM simulations of B_0 and B_1 into in operando cell development.

https://doi.org/10.5194/mr-2026-7
Preprint. Discussion started: 2 April 2026

Open Access MAGNETIC RESONANCE Discussions

To account for inhomogeneities of either B_0, i.e. Larmor frequencies , or B_1, i.e. rf fields, or both simultaneously, quantum optimal control (QOC) has established itself as a versatile NMR pulse design method, particularly after the emergence of computationally efficient, numerical QOC methods such as gradient ascent pulse engineering (GRAPE) (Khaneja et al., 2005). QOC has been used for customized pulse optimization, either with the goal to achieve robust broadband excitation covering extended ranges of inhomogeneities (Kobzar et al., 2004, 2008, 2012), selection of specific quantum coherence states (Köcher et al., 2016), or selective excitation or suppression of certain B_0-B_1 combinations (Kobzar et al., 2005). Ilott et al. (2014) have exploited the skin effect of metallic lithium, in this case the B_1 field attenuation and phase change originating from eddy currents, to achieve either selective excitation within the skin depth of the metal or a suppression of the metal signal.

In the present work, we combine FEM simulations and QOC pulse design to tailor rf pulses for selective excitation or suppression of NMR signals in the vicinity of metallic copper elements. We show that robust QOC pulses can still perform Larmor frequency selective excitation and suppression in the presence of conductive cell components. Furthermore, instead of just compensating for inhomogeneities, we introduce a new experimental approach, where the characteristic B_1 distortions in the proximity of conductive interfaces are exploited by B_1-selective QOC pulses to achieve spatial selectivity without the need for pulsed field gradients. The pulse performances are experimentally demonstrated on a test setup consisting of cavities between copper coins and between polymer coins with different solvents to mimic potential future applications in electrocatalysis with metal electrodes.

2 Experimental Methods and Simulations

2.1 Quantum Optimal Control Pulse Optimization

The QOC pulses were optimized using a Python implementation of the GRAPE algorithm (Khaneja et al., 2005) with numerical efficiency boosted by efficient spin control using analytical Lie algebraic derivatives (ESCALADE) (Foroozandeh and Singh, 2021; Goodwin and Vinding, 2023). The SciPy implementation of the limited-memory Broyden–Fletcher–Goldfarb–Shanno algorithm (L-BFGS-B) was chosen as optimization back end (Broyden, 1970; Fletcher, 1970; Goldfarb, 1970; Shanno, 1970; Byrd et al., 1995; Zhu et al., 1997; Virtanen et al., 2020). To facilitate selectivity with respect to B_0 and B_1, the concept of pattern pulses was used, a special variant of ensemble QOC where pulse optimization simultaneously runs across a whole ensemble of spin systems, each corresponding to a different combination of effective B_0 and B_1 (Kobzar et al., 2005). By assigning a target spin state $\boldsymbol{\rho}_{\mathrm{target}}$, corresponding to excitation or suppression, to each ensemble element, excitation patterns are achieved. Each ensemble element yields a quality factor computed as $\mathrm{Re}\left\langle \boldsymbol{\rho}_{\mathrm{target}} \middle| \boldsymbol{\rho}_{\mathrm{final}} \right\rangle$, the real part of the scalar product between the final spin state $\boldsymbol{\rho}_{\mathrm{final}}$ after applying the pulse and $\boldsymbol{\rho}_{\mathrm{target}}$. The total quality function optimized by L-BFGS-B was computed as weighted average of the ensemble quality factors. If not specified otherwise, the ensemble elements were weighted equally. The total control amplitude was limited by a hard upper bound of 10 kHz. Robustness with respect to B_0 variations was incorporated by variation of the Larmor frequencies ν_0, whereas robustness with respect to B_1 inhomogeneities was incorporated by allowing linear scalings of the nutation frequencies ν_1. The arising 2D grid of varying parameters is termed excitation profile. The excitation profile resolution was set to 41 ν_1 scalings times 401 ν_0 offsets. Considering the respective

https://doi.org/10.5194/mr-2026-7
Preprint. Discussion started: 2 April 2026

Open Access MAGNETIC RESONANCE Discussions

linear relation between B_0 and ν_0, as well as between B_1 and ν_1 (Hore, 2015)

$$\nu = -\frac{\gamma B}{2\pi}\,, \tag{1}$$

these terms are used interchangeably in the following unless an unambiguous distinction is required and stated. It must be noted that B_0 is used in this manuscript as the effective magnetic field that acts on a nuclear spin. That includes chemical (de-)shielding effects affecting the nucleus as well as susceptibility effects of any material in its environment. Thus, B_0, as used in this manuscript, may differ from the external, static magnetic field.

For the optimization of a B_0-selective excitation pulse, the excitation profile was chosen such that spins within a ν_0 range between -500 and 500 Hz are excited with $\boldsymbol{\rho}_{\mathrm{target}} = I_x$, whereas the remaining spins within the ν_0 range from -2 kHz to 2 kHz are suppressed, corresponding to $\boldsymbol{\rho}_{\mathrm{target}} = I_z$. Offsets outside of the selected bandwidth were not controlled. For a B_0-selective suppression pulse, the target states were swapped. The linear scaling factors of ν_1 ranged between 0.9 and 1.6. For the excitation pulse, a duration of 1 ms with 2000 equidistant time increments of 0.5 µs was sufficient to achieve a final mean quality factor of 94.9 %. For the suppression pulses, two distinct parameter sets were utilized: a duration of 1 ms with 2000 equidistant time increments of 0.5 µs (mean quality factor of 93.5 %), and a duration of 2 ms with 4000 equidistant time increments of 0.5 µs (mean quality factor of 95.6 %) to achieve a better frequency selectivity.

In the case of the suppression pulse, the quality factors of ensemble elements corresponding to a ν_0 between -250 and 250 Hz were weighted by a factor of 5 relative to the remaining fidelities. Furthermore, the quality factors of ensemble elements corresponding to a ν_1 scaling between 0.9 and 1.1 were additionally weighted by a factor of 5. This was due to the fact that the ensemble elements associated with these regions of the excitation profile tended to reach insufficient quality factor values for a homogeneous signal suppression. The pulse shapes and excitation profiles of the B_0-selective excitation and suppression pulses are visualized in Supporting Information (SI) Sec. 1.1 and 2.1 (Fig. S1 to S3 and S10 to S12), respectively.

B_1-selective pattern pulse excitation profiles were set up based on the increase in B_1 intensity around metallic elements. The increase was quantified by FEM simulations of the local B_1 field in the copper and polymer (represented by vacuum) cavities of the model setup following the procedure described in (Schatz et al., 2024). The simulated geometry is visualized in SI Sec. 3 (Fig. S19). The predicted relative B_1 increase is then determined as the ratio

$$\Gamma_{B_1} = \frac{B_1(\mathrm{Cu})}{B_1(\mathrm{vacuum})}\,. \tag{2}$$

For a given Γ_{B_1}, the excitation region in the profile is defined as the set of ensemble elements corresponding to $\Gamma_{B_1} \pm 0.1$. Ensemble elements in the excitation region are assigned $\boldsymbol{\rho}_{\mathrm{target}} = I_x$ and the remaining elements $\boldsymbol{\rho}_{\mathrm{target}} = I_z$. The ν_0 offset range was chosen from -1 kHz to 1 kHz. The range of ν_1 scalings was chosen from 0.9 to 1.6, except for the pulse for selective excitation at $\Gamma_{B_1} = 1.8$, where the maximum ν_1 scaling was raised to 1.9. A pulse duration of 1 ms with 2000 equidistant time increments of 0.5 µs was sufficient for all Γ_{B_1}. The obtained final quality factors are listed in Tab. 1. The pulse shapes and excitation profiles of the B_1-selective excitation and suppression pulses are visualized in SI Sec. 1.2 and 2.2 (Fig. S4 to S9 and S13 to S18), respectively.

https://doi.org/10.5194/mr-2026-7
Preprint. Discussion started: 2 April 2026

Open Access MAGNETIC RESONANCE Discussions

Table 1. Obtained final mean quality factors for the optimization of B_1-selective excitation pulses.

Γ_{B_1}	mean $\mathrm{Re}\langle \boldsymbol{\rho}_{\mathrm{target}} \vert \boldsymbol{\rho}_{\mathrm{final}} \rangle$
1.00	95.5 %
1.20	96.5 %
1.25	96.9 %
1.30	96.6 %
1.40	96.6 %
1.80	96.4 %

2.2 NMR Experiments

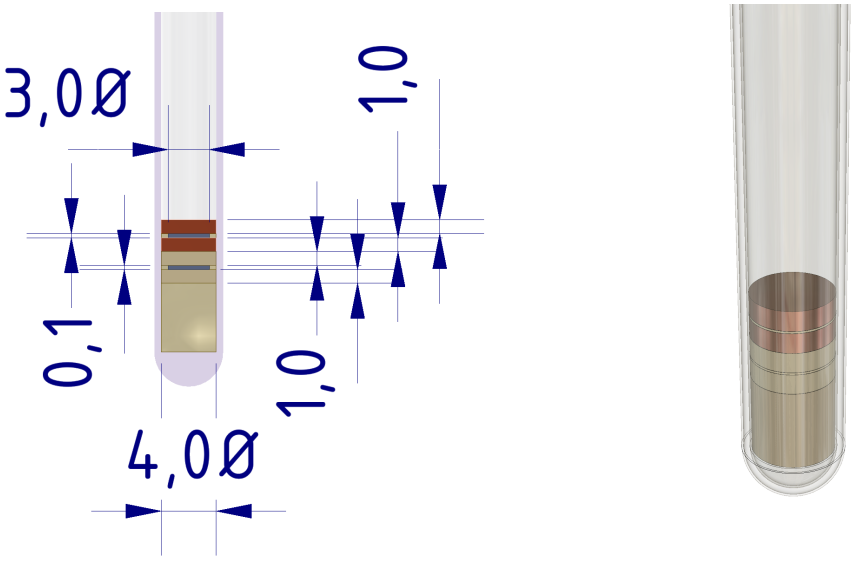

(a) (b)

Figure 1. Sectional side view of experimental setup with cell dimensions given in mm (a) and 3D illustration of setup inside a shortened standard 5 mm NMR tube (b). The cavities each have a diameter of 3 mm and a height of 0.1 mm. The coins each have a diameter of 4 mm and a height of 1 mm.

A model setup was prepared to demonstrate the operating principle of the developed QOC pulses. To investigate the field-distorting effects of conductive materials on liquid samples, the setup contained two cavities of equal dimensions; the first one in between two copper coins, the second one in between two polymer coins made of polyether ether ketone (PEEK) serving as lowly distorted reference cavity. The rotation axis of both cylindrical cavities and their coins were oriented parallel to the B_0 field and perpendicular to the B_1 field, according to the findings in a previous publication (Schatz et al., 2023). The model

https://doi.org/10.5194/mr-2026-7
Preprint. Discussion started: 2 April 2026

Open Access MAGNETIC RESONANCE Discussions

setup was fitted into a shortened common 5 mm NMR tube and is illustrated in Fig. 1a and 1b, including the diameter and thickness of copper and polymer coins as well as the polymer spacers which defined the size of the cavity. The NMR tube was shortened to remove the narrowed opening such that the entire tube has a diameter of 4 mm.

Liquids were only added in between two coins of equal material, limiting the maximum filling height of liquid in each cavity to 0.1 mm. *n*-dodecane (in copper cavity) and H_2O (in PEEK cavity) were chosen as non-mixable liquids, each of them filled into one of the two cavities, to enable an unambiguous distinction by spatial position as well as by their chemical shift. The model setup was positioned in the NMR tube such that the two cavities were placed around the center of the NMR-sensitive volume.

A Bruker DiffBB BBO broadband diffusion probe with magnetic field gradients along the B_0 direction (z-axis) with a maximum gradient strength of 2312 G/cm was operated on a Bruker Avance III HD spectrometer (Bruker BioSpin GmbH, Rheinstetten, Germany) with a 9.4 T wide-bore magnet.

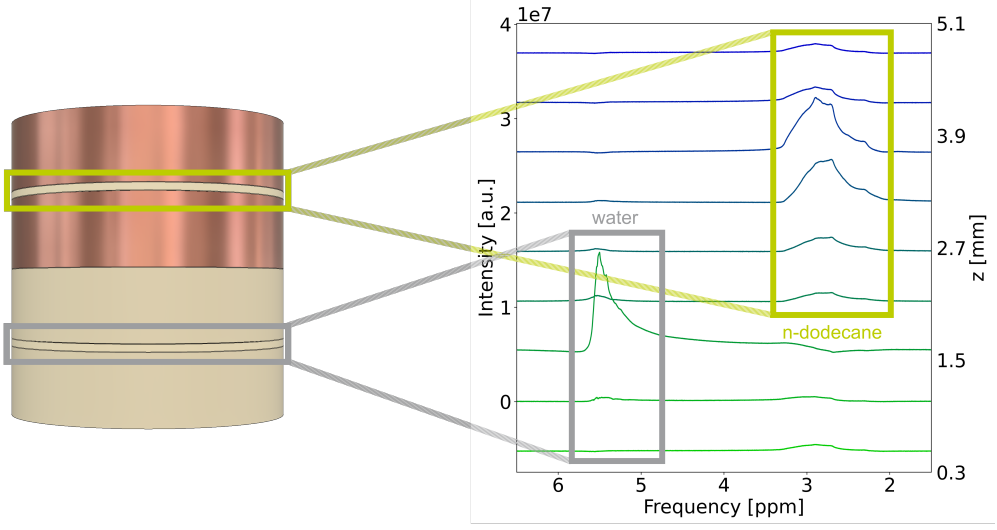

Figure 2. Spatially-encoded chemical shift imaging of H_2O and *n*-dodecane in between the double coins. The spatial position of the liquids can be differentiated on a scale of about half a mm.

The spatial position of the two liquids was verified by phase-encoded ^{1}H chemical shift imaging (CSI) along the z-axis (Fig. 2). Phase-encoded ^{1}H CSI was performed by using pulsed magnetic field gradients along z with a strength of $\pm$ 37.62 G/cm. The field of view was set to 20 mm with 32 points in the spatial dimension, resulting in a spatial resolution of 625 µm. The shim was adjusted for an optimal separation along the chemical shift axis in order to assign resonances unambiguously. No chemical shift reference was integrated in the model setup. Thus, the chemical shift of water and *n*-dodecane do not correspond to their tabulated values.

Standard FID-detected NMR experiments using a single hard pulse adjusted for a Bruker standard sample were compared to experiments where the hard pulse was substituted by QOC pulses. For the B_0-selective QOC pulses, in order to illustrate

https://doi.org/10.5194/mr-2026-7
Preprint. Discussion started: 2 April 2026


Open Access MAGNETIC RESONANCE Discussions

the selective bandwidth of 1000 Hz over the total pulse bandwidth of 4000 Hz, the ^{1}H resonance frequency offset $\Delta\nu_0$ was varied either in steps of 200 Hz or of 300 Hz, starting 600 Hz or 900 Hz downfield of the H_2O resonance for a total frequency range of 2200 Hz or of 2700 Hz, respectively. For the B_1-selective pulses, $\Delta\nu_0$ was set such that the total pulse bandwidth of 2000 Hz contained the resonances of both *n*-dodecane and H_2O. However, the pulse length required for a 90° pulse in this model setup differs from a Bruker standard sample. The actual 90° pulse lengths for each cavity were determined by a nutation experiment and the resonance integrals in all reference spectra were adjusted accordingly. The acquisition time was adjusted to record the full FID into the noise, and the relaxation delay was set to allow for complete relaxation. The baseline was corrected by using a splines fit.

Nutation experiments were performed with varying pulse length and a constant pulse power of 1.5 W. The pulse length list consisted of 100 points with a step size of 30 µs.

3 Results and Discussion

3.1 B_0 Selectivity

The B_0-selective QOC excitation pulses with a pulse length of 1 ms described in Sec. 2.1 were demonstrated in a proof-of-concept experiment on the model setup described in Sec. 2.2, with *n*-dodecane in the copper cavity and H_2O in the PEEK cavity. Fig. 3 illustrates the application of the B_0-selective pulses at selected offsets $\Delta\nu_0$. Here, $\Delta\nu_0$ was varied with a step size of 200 Hz between 2975 Hz and 775 Hz, with the excitation centered on either the resonance of H_2O at $\Delta\nu_0 = 2375$ Hz or on the resonance of *n*-dodecane at $\Delta\nu_0 = 1375$ Hz. A spectrum excited with a 90° hard pulse using the same setup was used as reference (denoted as standard, 1st spectrum from top), enabling the direct comparison between a hard pulse and the B_0-selective QOC pulses. The linewidth of the H_2O resonance (50 Hz) is smaller compared to the coalesced *n*-dodecane resonance (150 Hz). Both resonances show broad features, due to a non-optimal shim caused by the significant susceptibility differences throughout the model setup. The error on each individual resonance integral was calculated from the respective signal-to-noise ratio of each experiment.

When centering the excitation band on $\Delta\nu_0$ of either resonance, the QOC pulse achieved efficient excitation yielding a relative integral of 87.44 ± 0.43 % for H_2O or 115.34 ± 0.26 % for *n*-dodecane compared to the 90° hard pulse. Simultaneously, the respective other resonance was suppressed to either 4.96 ± 0.28 % or to 4.02 ± 0.40 % of its original value. The relative QOC integrals of both resonances compared to the reference for each of the B_0-selective pulses are summarized in SI Tab. S1.

Analogously, B_0-selective QOC suppression pulses with the same pulse length were applied with a $\Delta\nu_0$ step size of 300 Hz. These pulses (SI Fig. S27 and Tab. S2) efficiently suppressed the H_2O resonance to 7.42 ± 0.97 % of its original value. However, the *n*-dodecane resonance was only suppressed to 32.66 ± 0.32 %. This was due to an insufficient pulse performance at a duration of 1 ms, a non-optimal $\Delta\nu_0$ (+100 Hz) for *n*-dodecane in this specific experiment, and the large *n*-dodecane linewidth. To increase the suppression efficiency, the pulse duration was extended to 2 ms, and the step size was readjusted to 200 Hz such that the suppression band could be centered on *n*-dodecane or H_2O. As shown in Fig. 4 and SI Tab. S3, H_2O was suppressed to 1.01 ± 0.48 % and *n*-dodecane to 1.29 ± 0.26 % of their respective reference value when centering the

https://doi.org/10.5194/mr-2026-7
Preprint. Discussion started: 2 April 2026

Open Access MAGNETIC RESONANCE Discussions

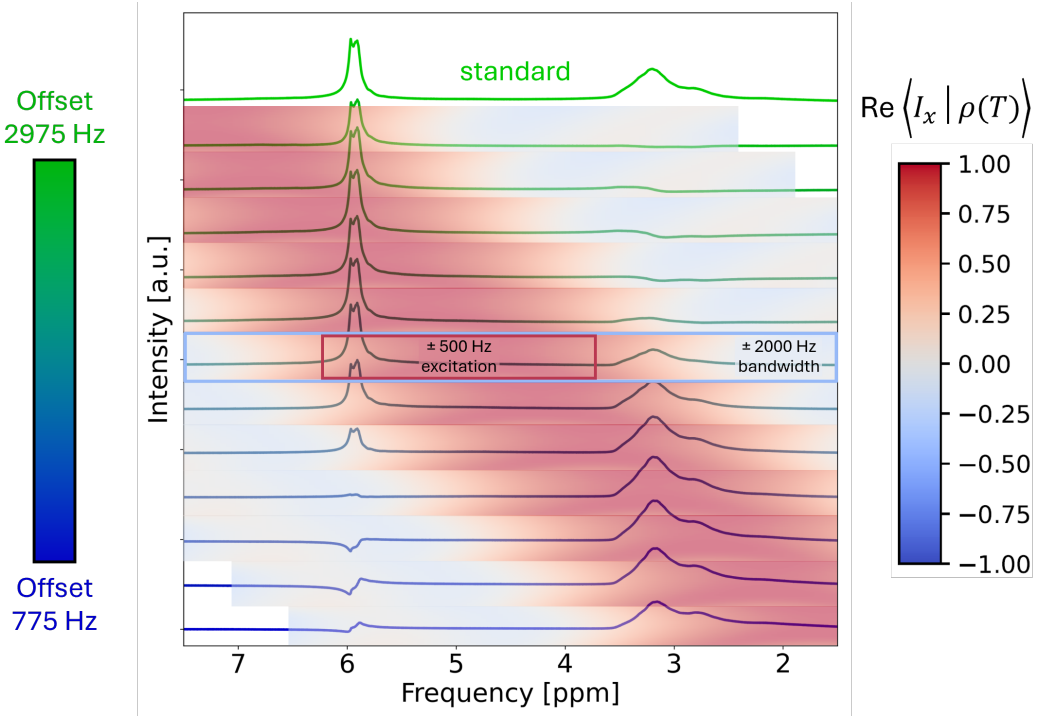

Figure 3. ^{1}H spectra recorded utilizing a B_0-selective excitation pulse with a selective excitation range of 2.5 ppm (±500 Hz), 1 ms duration, and a total frequency range of 4000 Hz applied at different $\Delta\nu_0$. The top spectrum depicts the reference ^{1}H spectrum recorded using a hard pulse. Hereby, the resonance at approx. 3 ppm is assigned to *n*-dodecane and the resonance at approx. 6 ppm to H_2O. The spectra recorded with QOC pulses are underlaid with colour gradients representing the theoretical x-magnetization $\mathrm{Re}\,\langle I_x|\rho(T)\rangle$ after applying the QOC pulse at each particular $\Delta\nu_0$ normalized to a range $[-1, 1]$. Selective excitation is achieved for the on-resonance pulses with $\Delta\nu_0 = 2375$ Hz for H_2O and $\Delta\nu_0 = 1375$ Hz for *n*-dodecane.

suppression band on either of them, yielding a significantly better suppression in the case of the 2 ms pulse and the adjusted step size. To gauge the signal selectivity of the QOC excitation pulses, a selectivity parameter

$$S_{\mathrm{QOC}}^{\mathrm{exc}} = \frac{\mathcal{I}_{\mathrm{exc}}(\mathcal{I}_{\mathrm{sup,ref}} - \mathcal{I}_{\mathrm{sup}})}{\mathcal{I}_{\mathrm{exc,ref}}\mathcal{I}_{\mathrm{sup,ref}}} \tag{3}$$

was defined, where $\mathcal{I}_{\mathrm{exc}}$ and $\mathcal{I}_{\mathrm{sup}}$ denote the integrals of the excited and suppressed resonances obtained by the QOC pulse, respectively. Analogously, $\mathcal{I}_{\mathrm{exc,ref}}$ and $\mathcal{I}_{\mathrm{sup,ref}}$ denote the integrals of the excited and suppressed resonances obtained by the 90° pulse, respectively. S_{QOC} should be between 0 and 1 in the ideal case that the 90° hard pulse reference achieves a uniform maximum excitation, with $S_{\mathrm{QOC}} = 1$ for an optimally selective and $S_{\mathrm{QOC}} = 0$ for a non-selective excitation. However, we observed QOC excitation surpassing the excitation of 90° hard pulses, thus achieving $S_{\mathrm{QOC}} > 1$ in some cases. We believe the origin of this effect lies within the capacitive interaction of the rf pulse and the conductive plates, which is more pronounced

https://doi.org/10.5194/mr-2026-7
Preprint. Discussion started: 2 April 2026

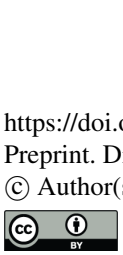

Open Access MAGNETIC RESONANCE Discussions

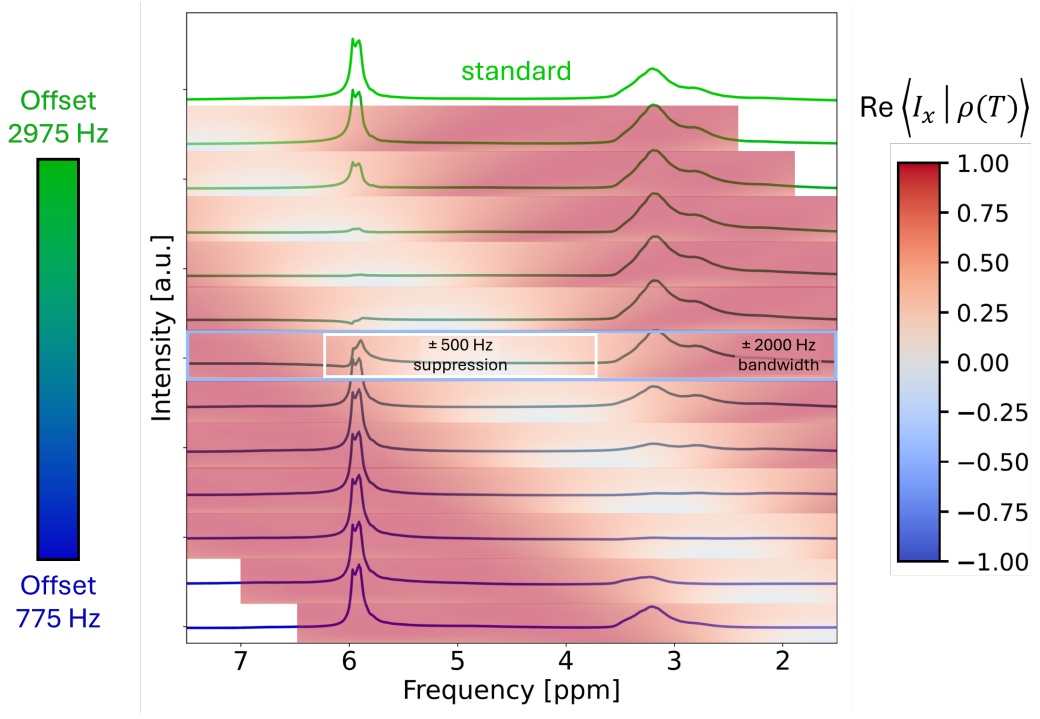

Figure 4. ^{1}H spectra recorded utilizing a B_0-selective suppression pulse with a selective suppression range of 2.5 ppm (±500 Hz), 2 ms duration, and a total frequency range of 4000 Hz applied at different $\Delta\nu_0$. The top spectrum depicts the reference ^{1}H spectrum recorded using a hard pulse. Hereby, the resonance at approx. 3 ppm is assigned to *n*-dodecane and the resonance at approx. 6 ppm to H_2O. The spectra recorded with QOC pulses are underlaid with colour gradients representing the theoretical x-magnetization $\mathrm{Re}\langle I_x|\rho(T)\rangle$ after applying the QOC pulse at each particular $\Delta\nu_0$ normalized to a range $[-1,1]$. Selective suppression is achieved for the on-resonance pulses with $\Delta\nu_0 = 2375$ Hz for H_2O and $\Delta\nu_0 = 1375$ Hz for *n*-dodecane.

for the short, hard pulse than for the long, soft QOC pulse. A corresponding selectivity parameter

$$S_{\mathrm{QOC}}^{\mathrm{sup}} = \frac{\mathcal{I}_{\mathrm{sup}}(\mathcal{I}_{\mathrm{exc,ref}} - \mathcal{I}_{\mathrm{exc}})}{\mathcal{I}_{\mathrm{exc,ref}}\mathcal{I}_{\mathrm{sup,ref}}} \tag{4}$$

was defined for QOC suppression pulses. In the following, S_{QOC} will be used to describe the selectivity of all QOC pulses, excitation as well as suppression, referring to their respective $S_{\mathrm{QOC}}^{\mathrm{exc}}$ or $S_{\mathrm{QOC}}^{\mathrm{sup}}$.

The highest S_{QOC} for B_0-selective excitation in Fig. 3 amounted to 1.202 ± 0.007 when positioning $\Delta\nu_0$ 200 Hz upfield from the center of the *n*-dodecane resonance ($\Delta\nu_0 = 1175$ Hz, 11th spectrum from top). This was slightly higher compared to $S_{\mathrm{QOC}} = 1.107 \pm 0.006$ when the pulse was exactly on-resonance ($\Delta\nu_0 = 1375$ Hz, 10th spectrum from top). Comparatively, selective suppression achieved a maximum S_{QOC} of 1.177 ± 0.008 with $\Delta\nu_0$ 200 Hz upfield from the center of the *n*-dodecane resonance, also slightly higher compared to $S_{\mathrm{QOC}} = 1.096 \pm 0.007$ when exactly on-resonance. Herein used excitation pulses achieved a similar maximum S_{QOC} as suppression pulses.

https://doi.org/10.5194/mr-2026-7
Preprint. Discussion started: 2 April 2026

Open Access MAGNETIC RESONANCE Discussions

The achievable S_{QOC} was strongly affected by $\Delta\nu_0$, even when staying in the pulse robustness range of $\pm$ 500 Hz. For example, S_{QOC} is reduced to 0.397 $\pm$ 0.004 and 0.839 $\pm$ 0.006 when moving $\Delta\nu_0$ either downfield ($\Delta\nu_0 =$ 1775 Hz, 8th spectrum from top) or upfield ($\Delta\nu_0 =$ 975 Hz, 12th spcetrum from top) by 400 Hz, respectively. S_{QOC} is also limited by the proximity of the suppressed and excited frequency ranges. The closer resonance frequencies are to each other, the more challenging a selective excitation or suppression via B_0-selective QOC pulses becomes, similar as for conventional selective pulses (McKay, 2009). A near-instant transition from excitation to suppression along the ν_0 dimension is difficult to realize in the pulse optimization and requires longer pulse durations for sharper transitions.

To overcome the selectivity difficulties for small frequency ranges, B_1 field variances originating from conductive materials were exploited instead of ν_0 differences in the optimization of QOC pulses.

3.2 B_1 Selectivity

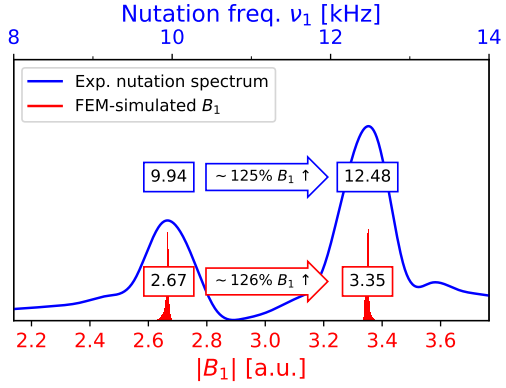

Figure 5. Experimental ν_1 spectrum interpolated by a cubic spline (blue) compared with FEM-simulated B_1 distribution (red). The smaller ν_1 and B_1 correspond to the PEEK cavity while the bigger ν_1 and B_1 correspond to the copper cavity. The relative difference between the ν_1 maxima (25.5 %) is in good alignment with the relative B_1 increase predicted by the FEM simulation (26.1 %).

The FEM-predicted ν_1 increase was validated experimentally via a nutation experiment (SI Fig. S20). A comparison of the obtained nutation frequencies for both cavities in the model setup is shown in Fig. 5.

The FEM simulations revealed two narrow, clearly separated B_1 distributions for the copper and PEEK cavity with $\Gamma_{B_1}^{\mathrm{FEM}} = 1.261$. The experimentally determined $\Gamma_{B_1}^{\mathrm{exp}}$ amounted to 1.255, resulting in a difference of 0.006 between simulation and experiment. A difference of this magnitude is negligible when applying QOC pulses due to their robustness with respect to B_1 inhomogeneities of $\pm$ 0.1. Exchanging H_2O by *n*-dodecane or other liquids affected neither the simulated nor experimentally determined Γ_{B_1} (SI Sec. 4.2.1). Thus, the difference in B_1 clearly originates from the surrounding material.

To exemplify the accuracy of the method, a range of QOC pulses for varying Γ_{B_1} (Sec. 2.1) was applied to the model setup and compared for a systematical screening of pulse effectiveness (Fig. 6). The errors on all values were calculated from the respective signal-to-noise ratio of each experiment. A standard spectrum with the same setup was used as reference, enabling

https://doi.org/10.5194/mr-2026-7
Preprint. Discussion started: 2 April 2026

Open Access MAGNETIC RESONANCE Discussions

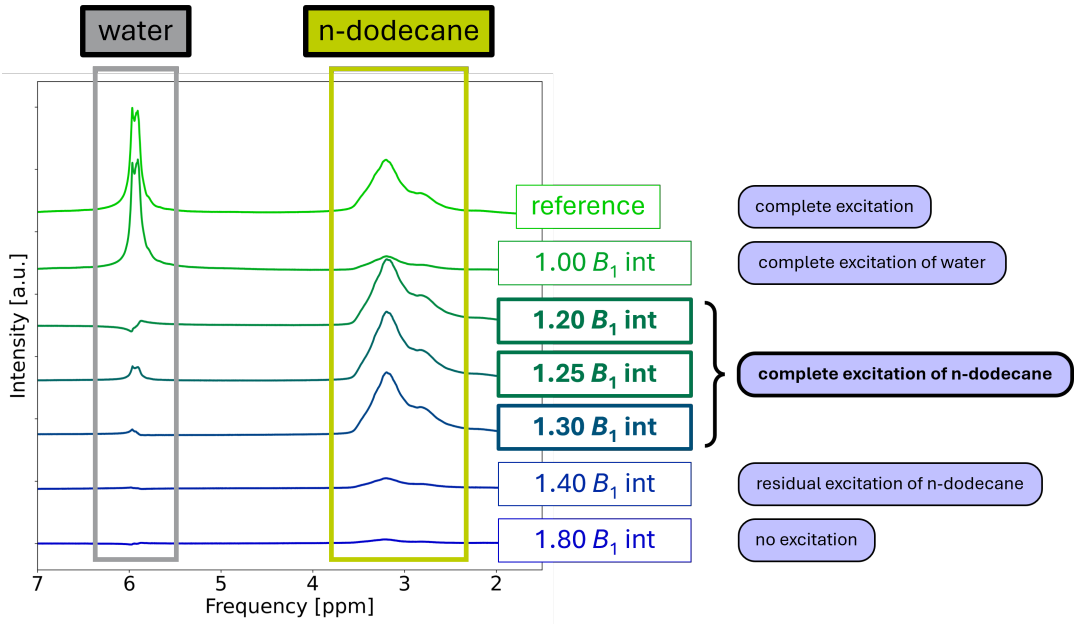

Figure 6. ^{1}H spectra recorded utilizing B_1-selective excitation pulses with a selective excitation range of $\Gamma_{B_1} \pm 0.1$, 1 ms duration, and a total frequency range of 2000 Hz. Hereby the resonance at approx. 3 ppm (framed in bright green) is assigned to *n*-dodecane and the resonance at approx. 6 ppm (framed in grey) to H_2O. The top spectrum depicts the reference ^{1}H spectrum recorded using a hard pulse. Below, spectra utilizing selective QOC pulses, optimized for increasing Γ_{B_1}, are displayed. Selective excitation of *n*-dodecane is achieved for $1.20 \leq \Gamma_{B_1} \leq 1.30$, which matches the B_1 amplification of the cavity in between copper.

the direct comparison between a 90° hard pulse and the Γ_{B_1}-selective QOC pulses. The relative excitation of both resonances compared to the reference for each of the B_1-selective pulses are summarized in Tab. 2. The QOC pulses for $\Gamma_{B_1} = 1.2$,

Table 2. Individual relative integral of the B_1-selective QOC excitation pulses compared to a corresponding 90° hard pulse.

Γ_{B_1}	H_2O excitation [%]	*n*-dodecane excitation [%]
1.00	99.79 ± 0.49	16.53 ± 0.30
1.20	7.76 ± 0.64	90.06 ± 0.40
1.25	11.57 ± 0.60	106.25 ± 0.37
1.30	3.10 ± 0.56	96.19 ± 0.46
1.40	0.73 ± 0.53	14.09 ± 0.33
1.80	1.11 ± 0.55	3.63 ± 0.34

$\Gamma_{B_1} = 1.25$ and $\Gamma_{B_1} = 1.3$ selectively excited the *n*-dodecane resonance to a minimum of 90.06 ± 0.49 % and simultaneously suppressed the resonance of H_2O to a maximum of 11.57 ± 0.60 %. These results confirm a successful QOC excitation of
220 resonances inside the copper cavity while suppressing resonances inside the PEEK cavitiy within the Γ_{B_1} robustness limit of

https://doi.org/10.5194/mr-2026-7
Preprint. Discussion started: 2 April 2026

Open Access MAGNETIC RESONANCE Discussions

$\pm$ 0.1. The highest excitation of *n*-dodecane was achieved with the pulse for $\Gamma_{B_1} = 1.25$ while the highest suppression of H_2O was achieved with the pulse for $\Gamma_{B_1} = 1.30$.

In comparison, the application of a QOC pulse optimized for $\Gamma_{B_1} = 1.0$ excited the H_2O resonance to 99.79 $\pm$ 0.49 % and suppressed the *n*-dodecane resonance to 16.53 $\pm$ 0.30 % of their original values. This illustrates that, depending on the Γ_{B_1} which the QOC pulses are optimized for, a resonance selectivity for either the copper cavity with increased B_1 or for the PEEK cavity with no B_1 increase can be achieved. Furthermore, the additional spectra corresponding to even higher Γ_{B_1} exemplify how a mismatch between the Γ_{B_1} range of the QOC pulse and the B_1 experienced by both investigated spins, leads to both resonances being suppressed to a maximum of 14.09 $\pm$ 0.33 % ($\Gamma_{B_1} = 1.4$) and 3.63 $\pm$ 0.34 % ($\Gamma_{B_1} = 1.8$) of their original values.

S_{QOC} was again determined to evaluate the effective signal selectivity of the B_1-selective QOC pulses and to compare it to the B_0-selective QOC pulses. Additionally, the experiments shown in Fig. 6 (except $\Gamma_{B_1} = 1.25$) were each repeated three times for the determination of a standard deviation. Thus, the standard deviation will be used instead of the error based on signal-to-noise to evaluate the QOC pulse performance in the following. The average S_{QOC} are summarized in Tab. 3. The

Table 3. Average S_{QOC} of the B_1-selective QOC excitation pulses. The corresponding 90° hard pulse has $S_{\mathrm{QOC}} = 0$.

Γ_{B_1}	S_{QOC}
1.00	0.941 $\pm$ 0.095
1.20	1.074 $\pm$ 0.232
1.30	0.959 $\pm$ 0.051
1.40	0.166 $\pm$ 0.040
1.80	0.029 $\pm$ 0.005

highest average S_{QOC} was found for $\Gamma_{B_1} = 1.2$ at 1.07 $\pm$ 0.23. For $\Gamma_{B_1} = 1.3$, the signal selectivity was on average slightly lower at $S_{\mathrm{QOC}} = 0.96 \pm 0.05$. Comparing the targeted Γ_{B_1} of these pulses suggests that the pulse for $\Gamma_{B_1} = 1.3$ should be more selective due to its Γ_{B_1} being slightly closer to the experimentally determined value of 1.255. The latter is, therefore, further away from the transition region of the QOC pulse, where excitation transits to suppression (SI Fig. S14 and S16). However, the S_{QOC} deviation between the pulses for $\Gamma_{B_1} = 1.2$ and $\Gamma_{B_1} = 1.3$ lies in the range of the error bars. Setting a different rf pulse center frequency, B_0 field shim or receiver gain was revealed to not affect the QOC spectra (SI Sec. 4.2.2 to 4.2.4), displaying additional QOC pulse flexibility when setting up experimental NMR parameters. By comparison, QOC pulses for Γ_{B_1} outside of the expected range result in a significantly lower average S_{QOC} of 0.166 ± 0.040 ($\Gamma_{B_1} = 1.4$) and 0.029 ± 0.005 ($\Gamma_{B_1} = 1.8$), thus the selectivity parameter S_{QOC} precisely and reproducibly expresses the QOC pulse selectivity.

4 Conclusions

In this work, a joint approach of B_1 simulation by FEM, numerical NMR pulse optimization by QOC, and the design of an electrochemically relevant model setup for in operando NMR was executed. B_1-robust, B_0-selective QOC pulses were

https://doi.org/10.5194/mr-2026-7
Preprint. Discussion started: 2 April 2026


Open Access MAGNETIC RESONANCE Discussions

able to selectively excite or suppress all resonances inside their selective ν_0 bandwidth, despite the presence of conductive cell components and the resulting B_1 distortions. The B_0 distortions, which were evident from the line broadening of the *n*-dodecane resonances, also did not affect the results of the QOC experiments, demonstrating how QOC can be an effective tool to compensate for magnetic field distortions caused by conductive cell components. Furthermore, B_1 field distortions near conductive electrochemical cell components in the model setup were accurately predicted by FEM and integrated into a QOC workflow to tailor pattern pulses which exploit the simulated sharp B_1 enhancement near conductive interfaces. Spins which experienced the predicted B_1 increase were selectively and abundantly excited by suitable pattern pulses, while other spins were predominantly suppressed with a selectivity matching the B_0-selective QOC. Therefore, this study shows that magnetic field distortions are not just mere obstacles, but that they can potentially be turned into exploitable features.

The selectivity parameter S_{QOC} was established and provided to compare the performance of QOC pulses. Although QOC pulses differed in their performance, each of them clearly proved that this integrated approach can yield spatially selective data, despite B_0 inhomogeneities and by taking advantage of strong B_1 field distortions. While selectivity can potentially be improved by increasing the duration of pattern pulses, it was shown that suitable contrast can be achieved with practically viable pulse durations for real-world conditions, where surface relaxation or the presence of transient paramagnetic species may prevent the use of longer, more selective pulses.

The proof-of-concept experiments also revealed fundamental insights into conventional selective NMR pulses in conductive systems. While B_0 distortions near electrodes or metal components appear prominent in spectra, their extent is minor (ppm range) in comparison to the B_1 distortions (% range), which were validated by experiment and FEM simulations. Thus, B_1 distortions can be much more readily and effectively exploited for spatially selective QOC pulse optimization compared to the utilization of B_0 artifacts, which are also affected by chemical (de-)shielding effects. Furthermore, this study also elucidates challenges of conventional solvent suppression methods in spectroelectrochemical NMR. The pulse sequences heavily rely on exact manipulation of the solvent magnetization, exploiting minute B_0 difference in the presence and absence of magnetic field gradients (Zheng and Price, 2010). With conductive materials, however, the large B_1 distortions disrupt the desired evolution of magnetization, as the conventional suppression pulses yield divergent flip angles due to changed nutation frequencies. In addition, even small B_0 distortions near metallic surfaces may cause off-resonance effects. While robust suppression schemes, such as continuous-wave (CW) irradiation, may dismiss B_1 distortions, they typically have a too narrow bandwidth to suppress susceptibility broadened signals and may even heat up the volume in proximity to a metal electrode.

For future studies, the QOC pulse design can be adapted to currently relevant questions in electrochemistry, such as the formation of intermediates on the electrode surface during CO_2 electrolysis or spatially selective investigations of the solid electrolyte interphase (SEI). Additionally, B_0 and B_1 selectivity of QOC pulses can be combined to achieve both, spatially and chemically-selective measurements, at the same time. To facilitate spatial selectivity at a precisely controlled level, electrodes can also be customized with specific surface adjustments which result in distinct, easily predictable B_0 and B_1 distortions. In conclusion, the combination of electrochemical in operando NMR, FEM simulations, and QOC pulse optimization enables new experimental approaches with the potential to gain insights into local electrochemical phenomena that have previously been inaccessible and may help answering complex research questions for which individual singular approaches might be

https://doi.org/10.5194/mr-2026-7
Preprint. Discussion started: 2 April 2026


Open Access MAGNETIC RESONANCE Discussions

insufficient. However, this workflow might be more difficult in the case of conductive materials with varying properties, such as porous electrodes or inhomogeneously distributed catalyst layers, requiring complex FEM simulations and exhibiting B_1 distortions that are changing during an experiment, which lead to broad and transiently changing B_1 field distributions. Nevertheless, the presented method allows for the non-invasive and selective investigation of molecules near metal surfaces with high component flexibility and can take advantage of the wide nucleus range NMR has to offer.

Data Availability

TopSpin raw data of the presented measurements and pulse sequences will be made available open access on the Jülich DATA repository at https://doi.org/10.26165/JUELICH-DATA/XQT0WN (Kochs et al., 2025) upon acceptance of the paper. The simulation/optimization codes used in this work and all other data are available from the authors upon request.

Author Contribution

Conception and design: JFK, AJR, MiS, SJ, SSK, and JG. Sample preparation and collection of data: JFK, and MiS. Optimal control implementation and optimization: AJR. FEM simulation: MaS. Analysis and interpretation of data: JFK, AJR, MiS, MaS, SJ, SSK, and JG. Supervision: SJ, RE, SSK, and JG. Manuscript preparation: JFK, AJR, MiS, MaS, SJ, SSK, and JG. Funding acquisition: RE, and JG Both JFK and AJR contributed equally to the publication and have the right to list their name first in their CV. All authors contributed to the article and approved the submitted version.

Competing Interests

The authors declare that they have no conflict of interest.

Acknowledgements

We thank Thomas Schulte-Herbrüggen from the Technical University of Munich and Burkhard Luy from Karlsruhe Institute of Technology for their input on ensemble quantum optimal control methods. We also thank Moritz Oberhauser and Matthias J. Brandl from the Bavarian NMR Center of the Technical University of Munich for fruitful exchange on intricacies of GRAPE implementations and for their help with implementing optimally controlled NMR experiments. Funding by the German Research Foundation (DFG) under Germany's Excellence Strategy – Cluster of Excellence 2186 "The Fuel Science Center" (grant no. 390919832), and by the German Federal Ministry of Research, Technology and Space (BMFTR) within the H_2Giga project DERIEL (grant number 03HY122C) is gratefully acknowledged.

https://doi.org/10.5194/mr-2026-7
Preprint. Discussion started: 2 April 2026

Open Access MAGNETIC RESONANCE Discussions

References

Aguilera, A. R., MacMillan, B., Krachkovskiy, S., Sanders, K. J., Alkhayri, F., Adam Dyker, C., Goward, G. R., and Balcom, B. J.: A parallel-plate RF probe and battery cartridge for ^{7}Li ion battery studies, J. Magn. Reson., 325, 106 943, https://doi.org/10.1016/j.jmr.2021.106943, 2021.

Bommarito, G. M., Acevedo, D., and Abruna, H. D.: In situ monitoring of electrochemically induced roughening with the crystal truncation rod technique, J. Phys. Chem., 96, 3416–3419, https://doi.org/10.1021/j100187a044, 1992.

Broyden, C. G.: The convergence of a class of double-rank minimization algorithms 1. General considerations, IMA J. Appl. Math., 6, 76–90, https://doi.org/10.1093/imamat/6.1.76, 1970.

Byrd, R. H., Lu, P., Nocedal, J., and Zhu, C.: A limited memory algorithm for bound constrained optimization, SIAM J. Sci. Comput., 16, 1190–1208, https://doi.org/10.1137/0916069, 1995.

Corson, E. R., Kas, R., Kostecki, R., Urban, J. J., Smith, W. A., McCloskey, B. D., and Kortlever, R.: In situ ATR-SEIRAS of carbon dioxide reduction at a plasmonic silver cathode, J. Am. Chem. Soc., 142, 11 750–11 762, https://doi.org/10.1021/jacs.0c01953, 2020.

Faid, A. Y., Barnett, A. O., Seland, F., and Sunde, S.: Ni/NiO nanosheets for alkaline hydrogen evolution reaction: In situ electrochemical-Raman study, Electrochim. Acta, 361, 137 040, https://doi.org/10.1016/j.electacta.2020.137040, 2020.

Fletcher, R.: A new approach to variable metric algorithms, Comput. J., 13, 317–322, https://doi.org/10.1093/comjnl/13.3.317, 1970.

Foroozandeh, M. and Singh, P.: Optimal control of spins by analytical Lie algebraic derivatives, Automatica, 129, 109 611, https://doi.org/https://doi.org/10.1016/j.automatica.2021.109611, 2021.

Goldfarb, D.: A family of variable-metric methods derived by variational means, Math. Comput., 24, 23–26, https://doi.org/10.1090/S0025-5718-1970-0258249-6, 1970.

Goodwin, D. L. and Vinding, M. S.: Accelerated Newton-Raphson GRAPE methods for optimal control, Phys. Rev. Res., 5, L012 042, https://doi.org/10.1103/PhysRevResearch.5.L012042, 2023.

Hamann, C. H. and Vielstich, W.: Elektrochemie, Wiley-VCH, 4th edn., ISBN 978-3-527-31068-5, 2005.

Holtz, M. E., Yu, Y., Gunceler, D., Gao, J., Sundararaman, R., Schwarz, K. A., Arias, T. A., Abruña, H. D., and Muller, D. A.: Nanoscale imaging of lithium ion distribution during in situ operation of battery electrode and electrolyte, Nano Lett., 14, 1453–1459, https://doi.org/10.1021/nl404577c, 2014.

Hore, P. J.: Nuclear Magnetic Resonance, Oxford Chemistry Primers, Oxford University Press, Oxford, 2nd edn., ISBN 9780198703419, 2015.

Huang, X., Plaza, M., Ko, J. Y. P., Abruña, H. D., and Brock, J. D.: Relaxation of asymmetric crystallographic tilt: In situ X-ray diffraction studies of epitaxial electrodeposition of bismuth on GaAs (110), J. Appl. Phys., 124, 035 301, https://doi.org/10.1063/1.5026630, 2018.

Ilott, A. J. and Jerschow, A.: Super-resolution surface microscopy of conductors using magnetic resonance, Sci. Rep., 7, 5425, https://doi.org/10.1038/s41598-017-05429-3, 2017.

Ilott, A. J., Chandrashekar, S., Klöckner, A., Chang, H. J., Trease, N. M., Grey, C. P., Greengard, L., and Jerschow, A.: Visualizing skin effects in conductors with MRI: ^{7}Li MRI experiments and calculations, J. Magn. Reson., 245, 143–149, https://doi.org/10.1016/j.jmr.2014.06.013, 2014.

Jovanovic, S., Schleker, P. P. M., Streun, M., Merz, S., Jakes, P., Schatz, M., Eichel, R.-A., and Granwehr, J.: An electrochemical cell for in operando ^{13}C nuclear magnetic resonance investigations of carbon dioxide/carbonate processes in aqueous solution, Magn. Reson., 2, 265–280, https://doi.org/10.5194/mr-2-265-2021, 2021.

https://doi.org/10.5194/mr-2026-7
Preprint. Discussion started: 2 April 2026

Open Access MAGNETIC RESONANCE Discussions

Khaneja, N., Reiss, T., Kehlet, C., Schulte-Herbrüggen, T., and Glaser, S. J.: Optimal control of coupled spin dynamics: design of NMR pulse sequences by gradient ascent algorithms, J. Magn. Reson., 172, 296–305, https://doi.org/10.1016/j.jmr.2004.11.004, 2005.

Kobzar, K., Skinner, T. E., Khaneja, N., Glaser, S. J., and Luy, B.: Exploring the limits of broadband excitation and inversion pulses, J. Magn. Reson., 170, 236–243, https://doi.org/10.1016/j.jmr.2004.06.017, 2004.

Kobzar, K., Luy, B., Khaneja, N., and Glaser, S. J.: Pattern pulses: design of arbitrary excitation profiles as a function of pulse amplitude and offset, J. Magn. Reson., 173, 229–235, https://doi.org/10.1016/j.jmr.2004.12.005, 2005.

Kobzar, K., Skinner, T. E., Khaneja, N., Glaser, S. J., and Luy, B.: Exploring the limits of broadband excitation and inversion: II. Rf-power optimized pulses, J. Magn. Reson., 194, 58–66, https://doi.org/10.1016/j.jmr.2008.05.023, 2008.

Kobzar, K., Ehni, S., Skinner, T. E., Glaser, S. J., and Luy, B.: Exploring the limits of broadband 90° and 180° universal rotation pulses, J. Magn. Reson., 225, 142–160, https://doi.org/10.1016/j.jmr.2012.09.013, 2012.

Köcher, S. S., Heydenreich, T., Zhang, Y., Reddy, G. N. M., Caldarelli, S., Yuan, H., and Glaser, S. J.: Time-optimal excitation of maximum quantum coherence: Physical limits and pulse sequences, J. Chem. Phys., 144, 164 103, https://doi.org/10.1063/1.4945781, 2016.

Lee, S., Moysiadou, A., Chu, Y.-C., Chen, H. M., and Hu, X.: Tracking high-valent surface iron species in the oxygen evolution reaction on cobalt iron (oxy)hydroxides, Energy Environ. Sci., 15, 206–214, https://doi.org/10.1039/D1EE02999A, 2022.

McKay, R. T.: Recent advances in solvent suppression for solution NMR: A practical reference, in: Annual Reports on NMR Spectroscopy, edited by Webb, G., vol. 66 of *Annual Reports on NMR Spectroscopy*, pp. 33–76, Academic Press, ISBN 978-0-12-374737-2, https://doi.org/10.1016/S0066-4103(08)00402-X, 2009.

Mohammadi, M. and Jerschow, A.: In situ and operando magnetic resonance imaging of electrochemical cells: A perspective, J. Magn. Reson., 308, 106 600, https://doi.org/10.1016/j.jmr.2019.106600, 2019.

Pecher, O., Carretero-Gonzalez, J., Griffith, K. J., and Grey, C. P.: Materials' methods: NMR in battery research, Chem. Mater., 29, 213–242, https://doi.org/10.1021/acs.chemmater.6b03183, 2017.

Richards, J. A. and Evans, D. H.: Flow cell for electrolysis within the probe of a nuclear magnetic resonance spectrometer, Anal. Chem., 47, 964–966, https://doi.org/10.1021/ac60356a016, 1975.

Sanders, K. J., Aguilera, A. R., Keffer, J. R., Balcom, B. J., Halalay, I. C., and Goward, G. R.: Transient lithium metal plating on graphite: Operando ^{7}Li nuclear magnetic resonance investigation of a battery cell using a novel RF probe, Carbon, 189, 377–385, https://doi.org/10.1016/j.carbon.2021.12.082, 2022.

Schatz, M., Jovanovic, S., Eichel, R.-A., and Granwehr, J.: Quantifying local pH changes in carbonate electrolyte during copper-catalysed Formula: see text electroreduction using in operando formula, Sci. Rep., 12, 8274, https://doi.org/10.1038/s41598-022-12264-8, 2022.

Schatz, M., Kochs, J. F., Jovanovic, S., Eichel, R.-A., and Granwehr, J.: Interplay of local pH and cation hydrolysis during electrochemical CO_2 reduction visualized by in operando chemical shift-resolved magnetic resonance imaging, J. Phys. Chem. C, 127, 18 986–18 996, https://doi.org/10.1021/acs.jpcc.3c03563, 2023.

Schatz, M., Streun, M., Jovanovic, S., Eichel, R.-A., and Granwehr, J.: Workflow for systematic design of electrochemical in operando NMR cells by matching B_0 and B_1 field simulations with experiments, Magn. Reson., 5, 167–180, https://doi.org/10.5194/mr-5-167-2024, 2024.

Shanno, D. F.: Conditioning of quasi-Newton methods for function minimization, Math. Comput., 24, 647–656, https://doi.org/10.1090/S0025-5718-1970-0274029-X, 1970.

Vashaee, S., Goora, F., Britton, M. M., Newling, B., and Balcom, B. J.: Mapping B_1-induced eddy current effects near metallic structures in MR images: a comparison of simulation and experiment, J. Magn. Reson., 250, 17–24, https://doi.org/10.1016/j.jmr.2014.10.016, 2015.

https://doi.org/10.5194/mr-2026-7
Preprint. Discussion started: 2 April 2026

Open Access MAGNETIC RESONANCE Discussions

Virtanen, P., Gommers, R., Oliphant, T. E., Haberland, M., Reddy, T., Cournapeau, D., Burovski, E., Peterson, P., Weckesser, W., Bright, J., van der Walt, S. J., Brett, M., Wilson, J., Millman, K. J., Mayorov, N., Nelson, A. R. J., Jones, E., Kern, R., Larson, E., Carey, C. J., Polat, İ., Feng, Y., Moore, E. W., VanderPlas, J., Laxalde, D., Perktold, J., Cimrman, R., Henriksen, I., Quintero, E. A., Harris, C. R., Archibald, A. M., Ribeiro, A. H., Pedregosa, F., van Mulbregt, P., and SciPy 1.0 Contributors: SciPy 1.0: Fundamental algorithms for scientific computing in Python, Nat. Methods, 17, 261–272, https://doi.org/10.1038/s41592-019-0686-2, 2020.

Walder, B. J., Conradi, M. S., Borchardt, J. J., Merrill, L. C., Sorte, E. G., Deichmann, E. J., Anderson, T. M., Alam, T. M., and Harrison, K. L.: NMR spectroscopy of coin cell batteries with metal casings, Sci. Adv., 7, eabg8298, https://doi.org/10.1126/sciadv.abg8298, 2021.

Williamson, M. J., Tromp, R. M., Vereecken, P. M., Hull, R., and Ross, F. M.: Dynamic microscopy of nanoscale cluster growth at the solid-liquid interface, Nat. Mater., 2, 532–536, https://doi.org/10.1038/nmat944, 2003.

Wolff, B., Schleker, P. P. M., Ditler, H., Rahe, C., Hetzke, T., Jakes, P., Eichel, R.-A., and Granwehr, J.: In operando EPR and NMR cell for correlative characterisation of battery electrodes, ChemRxiv [preprint], https://doi.org/10.26434/chemrxiv-2025-g1sv5, 2025.

Zhang, Z., Marble, A. E., MacGregor, R. P., Martin, J., Wang, H., and Balcom, B. J.: Zero-mode TEM parallel-plate resonator for high-resolution thin film magnetic resonance imaging, Can. J. Chem., 89, 745–753, https://doi.org/10.1139/v11-018, 2011.

Zheng, G. and Price, W. S.: Solvent signal suppression in NMR, Prog. Nucl. Magn. Reson. Spectrosc., 56, 267–288, https://doi.org/10.1016/j.pnmrs.2010.01.001, 2010.

Zhu, C., Byrd, R. H., Lu, P., and Nocedal, J.: Algorithm 778: L-BFGS-B: Fortran subroutines for large-scale bound-constrained optimization, ACM Trans. Math. Softw., 23, 550–560, https://doi.org/10.1145/279232.279236, 1997.

Zoski, C. G.: Handbook of Electrochemistry, Elsevier, Amsterdam and Boston, 1st edn., ISBN 9780444519580, https://doi.org/10.1016/B978-0-444-51958-0.X5000-9, 2007.